An improved parametric level set method for structural frequency response optimization problems

LiHao[a, b]

LuoZhen[b, *]

zhen.luo@uts.edu.au

GaoLiang[a, *]

gaoliang@mail.hust.edu.cn

WuJinglai[a]

[a]State Key Lab of Digital Manufacturing Equipment and Technology Huazhong University of Science and Technology, 1037 Luoyu Road, Wuhan, Hubei 430074, China

[b]School of Electrical, Mechanical and Mechatronic Systems The University of Technology, Sydney, 15 Broadway, Ultimo, NSW 2007, Australia

*Corresponding authors.

Abstract

In conventional parametric level set methods, the compactly supported radial basis functions (CSRBF) are used to approximate the level set function due to their unique properties, such as the sparsity of the interpolation matrix. The CSRBFs only consider the contributions of knots within a narrow sub-region, which sacrifices accuracy for efficiency in the interpolation. However, the accuracy loss in the CSRBF-based method may prolong the iteration and gradually lead the topology optimization towards a worse local optimum or even an unfeasible design, especially when the allowable material usage in the design domain is relatively low. This will significantly affect the performance of the optimization method. This paper proposes an improved parametric level set method (iPLSM), which is more efficient and effective in topology optimization designs. In this method, the Gaussian radial basis function with global support is used to parameterize the level set surface, to ensure a high numerical accuracy due to the consideration of all interpolation knots in the global domain. Then, a discrete wavelet transform scheme is incorporated into the parametric form to compress the full interpolation matrix and save the computational cost. The proposed method is applied to both the global and local frequency response optimization problems under wide excitation frequency ranges, to validate its efficiency and effectiveness.

Keywords: Topology optimization; Level set method; Gaussian radial basis function; Discrete wavelet transform; Frequency response optimization

1 Introduction

Structural topology optimization is capable of determining the best layout of material in the design domain, so as to optimize concerned structural performances under the given constraints. It has gained extensive interests in both academia and industry. One fundamental theory in this field was established by Michell [1]. In his work, the exact solutions for some truss structures were presented by using the analytical method. However, these truss structure design problems only consider single load case and depend on the appropriate specification of strains [2]. Later, Cox [3], Hemp and Chan [4–6], Prager and Rozvany [7], Cheng and Olhoff [8,9] and other researchers further developed the Michell theory for more general topology-related layout optimizations. These studies reveal that topology optimization can pave a new pathway to provide solutions for many real-world engineering optimization problems [10,11]. Up till now, several different methods have been established for topology optimization, such as the homogenization method [12], the solid isotropic material with penalization (SIMP) [13,14], the evolutionary structural optimization (ESO) method [15], as well as the level set method (LSM) [16–20], which are applied to a broad range of structure and material design problems [11,21].

LSM has recently emerged as an efficient design tool for shape and topology optimization of structures [16,17]. One of the fundamental concepts behind the LSM is to implicitly embed the lower dimensional design boundary of a structure into a higher dimensional level set function (LSF) [18], and the merging and splitting of structural boundary (zero level set) lead to the shape and topology changes. The propagation of the level set function is mathematically governed by the Hamilton-Jacobi partial differential equation (H-J PDE) [19, 20,22]. After one of the pioneer works [17], the level set methods are gradually becoming popular [19,20] and have been applied to several different design problems [22–29], due to their unique favorable features, e.g. smooth boundary and concise interface in geometry, flexibility of shape and topological changes, and simultaneous shape and topology optimization [19,20].

Despite the above advantages, several defects of the most classic LSM may significantly affect its efficiency. Firstly, the level set surface may become too flat or too steep during optimization, and the flatness or the steepness will lead to unfavorable numerical issues [19,20]. Thus, an extra re-initialization operation is often used to reshape the LSF to be a signed-distance function at each iteration, which will cause additional computer time. Secondly, the Courant–Friedrichs–Lewy (CFL) condition should be satisfied to keep the stability of the up-wind scheme [21]. This means the time step in the explicit scheme should be small enough, and thus more iterations are required to achieve an optimal design. Thirdly, in the standard LSM, the normal velocity field needs to be extended from the boundary to the whole domain or a narrow band along the boundary [17], and the velocity extension often requires extra computational effort. More importantly, many efficient and well-developed structural topology optimization algorithms [13,30] cannot be directly used in the conventional LSM.

Therefore, several alternative LSMs [31–37] have been developed to overcome the above unfavorable features. Among these approaches, the parametric level set method (PLSM) [35–37] has shown its capacity in simultaneously maintaining the unique features while eliminating the numerical issues of the most conventional LSM. The key concept of the PLSM is to interpolate the original level set surface via a given set of radial basis functions (RBFs) positioned at fixed knots inside the design domain. In this sense, the solution of a system of the H-J PDEs is changed to the solution of a number of algebraic equations, only with the unknown expansion coefficients of the RBF interpolation to be iteratively updated. Therefore, the most challenging topology optimization problem is converted to a relatively easy “size” optimization problem. In particular, the PLSM can directly integrate with the more efficient gradient-based optimization algorithms, such as the optimality criteria (OC) [13] and mathematical programming methods [30], which can't be easily applied to the conventional LSMs.

The efficiency and accuracy of the RBF interpolation will significantly influence the PLSM-based optimization. In the conventional PLSMs [35-37], compactly supported RBF (CSRBF) [38,39] is popularly used to approximate the LSF, due to its sparse interpolation matrix. Actually, the support of CSRBF is a limited sub-domain around a sample knot, and thus not all the interpolation knots are included to approximate the LSF at that sample knot. In other words, it sacrifices the interpolation accuracy for efficiency by ignoring a number of interpolation knots that are outside a predefined sub-region. The accumulated accuracy loss over iterations will eventually lead the optimization to a local optimum with lower performance or even an unfeasible design, especially when the allowable material usage in the design domain is relatively low. Comparing with the CSRBFs, the globally supported RBFs (GSRBFs) use all the interpolation knots to calculate the LSF value at each sample knot, and thus can guarantee a higher interpolation accuracy [38] to obtain a higher-performance design. However, the full interpolation matrix will considerably increase the computation effort. Indeed, a compressed interpolation matrix will be a reasonable solution to this computational difficulty.

Discrete wavelet transform (DWT) is a multi-resolution decomposition method for input data and has been widely used in signal processing, image compression, computer vision and denoising [40]. It can be used to handle the fully populated matrices [40,41], because of the capability of rapidly capturing the critical information from a large-scale and scattered data set. In brief, it can compress a full matrix into a much sparser one with negligible impact upon the computational accuracy. Therefore, the main contribution of this study is to firstly propose an improved parametric level set method (iPLSM) based on incorporation of the DWT and GSRBF-based interpolation, so as to further improve the efficiency and effectiveness of topological shape optimization.

Structural dynamic response optimization has received much attention in engineering [42–46]. This study will focus on the structural frequency response optimization [8,47], which aims to minimize the response under external excitations at the specific parts of a structure or over the entire structure. A number of studies have been made to deal with the frequency optimization problems under a single excitation frequency [8,47–52]. In engineering, however, a dynamic structure is always subject to an excitation frequency range. One critical issue for topology optimization under the excitation frequency range is the prohibitive computation cost caused by the repetitive finite element (FE) simulation calls. Hence, the model reduction (MR) technique [47] is essential to reduce the degrees of freedom (size) of the system during the FE procedure. For instance, Jensen [53] applied the Padé approximation to calculate the frequency response over the wide excitation frequency domain. Yoon [54] compared the performances of different MR schemes in dynamic structural analysis. More recently, Shu et al. [55], Rong et al. [56] and Liu et al. [57] also investigated the frequency response optimization problems subject to excitation frequency ranges. Nevertheless, most studies are based on the elemental density distribution approaches, which may have difficulties in capturing the structural boundary in geometry. Actually, a clear structural geometry is important and will greatly facilitate the optimized design to be directly integrated into the commercial software for analysis or manufacture purposes.

Hence, this paper develops an efficient iPLSM for structural frequency response optimizations under the given excitation frequency ranges. In this method, the Gaussian RBF with global support is used to parameterize the LSM. A matrix compression scheme, termed as DWT, is firstly integrated into the parameterization framework to reduce the nonzero elements in the Gaussian RBF-based interpolation matrix. By this means, all the positive features of the LSM can be maintained, while the unfavorable numerical issues of the classic LSM can be avoided. More importantly, the computational time of iPLSM can be remarkably reduced, while the higher-performance designs can be achieved when comparing with the conventional PLSM [35–37]. To verify the efficiency and effectiveness of the proposed method, both the local frequency response optimization (non-self adjoint problem) and dynamic compliance optimization (self adjoint problem) within wide excitation frequency ranges are investigated.

2 Improved parametric level set method

2.1 Boundary representation and geometry mapping by LSM

The fundamental of LSM is to embed the structural boundary implicitly as the zero iso-surface of a higher dimensional scalar function with Lipschitz continuity, as shown in Fig. 1. Considering a fixed Eulerian reference domain

D that contains the solid, boundary and void, different parts within D can be represented by the LSF Φ:

$$\begin{cases} \Phi(\mathbf{x},t) > 0, & \forall \mathbf{x} \in \Omega \setminus \Gamma \quad (solid\ region) \\ \Phi(\mathbf{x},t) = 0, & \forall \mathbf{x} \in \Gamma \quad (boundary) \\ \Phi(\mathbf{x},t) < 0, & \forall \mathbf{x} \in D \setminus \Omega \quad (void\ region) \end{cases} \tag{1}$$

where $\mathbf{x}$ denote the spatial variables (coordinates of level set grids) in domain D. t denotes the pseudo time variable. Ω denotes all the admissible shapes, and Γ is the structural boundary. It is noted that Γ contains the Dirichlet boundary Γ_D, Neumann boundary Γ_N and traction free boundary Γ_F:

$$\Gamma = \Gamma_D \cup \Gamma_N \cup \Gamma_F \tag{2}$$

Another important part of the level-set-based topology optimization is the mapping of the boundary geometry to a mechanical model. Normally, the boundary description (1) can be expressed in terms of the exact Heaviside function $H(\Phi)$, so as to formulate integrals of some functional J over the material domain [17,19–21]:

$$\int_{\Omega} J dV = \int_{D} J \cdot H(\Phi)\, dV \tag{3}$$

where

$$H(\Phi) = \begin{cases} 1, \Phi \geq 0 \\ 0, \Phi < 0 \end{cases} \tag{4}$$

and dV indicates a volume integral.

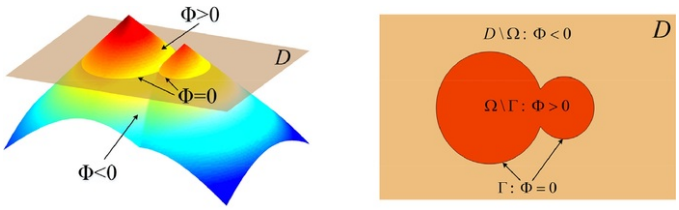

Fig. 1 (a) 3D level set surface and (b) 2D design domain.

alt-text: Fig. 1.

In the field of topology optimization, the integral in (3) can be approximately calculated by using the finite element method (FEM) on a fixed regular mesh. However, in the LSM, the standard FEM may fail to evaluate the integrals of those elements cut by the moving boundary [19,20]. A simple way to tackle this issue is the “ersatz material” approach [20,21]. It assumes that the element strain and stiffness are approximately proportional to the material fraction of that element (i.e. pseudo element density), while the void elements are filled with weak material to avoid singularity. Thus, the volume integral of functional J can be approximated by the FEM:

$$\int_{D} J \cdot H(\Phi)\, dV \approx \int_{D} J \cdot \widetilde{H}(\Phi)\, dV \approx \sum_{h=1}^{NE} \chi_h(\Phi) \int_{D_h} J dV, h = 1, 2, ..., NE \tag{5}$$

where h denotes a single element in domain D, and D_h represents the design domain of an element. NE is the total number of finite elements. Due to the fact that the exact Heaviside function in (4) is not differentiable, an approximate Heaviside function $\widetilde{H}(\Phi)$ (smooth and differentiable) can be used to replace $H(\Phi)$ during topology optimization [21]:

$$\widetilde{H}(\Phi) = \frac{1}{2}\left(1 + \frac{2}{\pi}\arctan\left(\frac{\Phi}{\gamma}\right)\right) \tag{6}$$

and the approximate Dirac delta function is given by:

$$\widetilde{\delta}(\Phi) = \frac{\partial \widetilde{H}(\Phi)}{\partial \Phi} = \frac{1}{\pi} \cdot \frac{\gamma}{\Phi^2 + \gamma^2} \tag{7}$$

where γ is a small positive constant that is equal to $2 \bullet \Delta$ [36]. In this study, Δ denotes the edge length of a fixed regular level set grid. Then, the pseudo element density can be defined by:

$$\chi_h(\Phi) = \tau + (1-\tau)\frac{\int_{D_h}\widetilde{H}(\Phi)\,dV}{\int_{D_h}dV} \tag{8}$$

where τ=0.001 is introduced to avoid singular problems. The integral of over D_h in (8) can be calculated numerically by the Gauss quadrature, when a number of equally spaced integration points are allocated in each element cut by the moving boundary [21]. In this case, the following integral can be also approximately calculated by FEM:

$$\int_D J\cdot\widetilde{\delta}(\Phi)\,dV \approx \sum_{h=1}^{NE}\frac{\partial\chi_h(\Phi)}{\partial\Phi}\cdot\int_{D_h}JdV = \sum_{h=1}^{NE}(1-\tau)\frac{\int_{D_h}\widetilde{\delta}(\Phi)\,dV}{\int_{D_h}dV}\cdot\int_{D_h}JdV, h=1,2,...,NE \tag{9}$$

2.2 Parameterization of LSM using Gaussian RBF

In this paper, the original LSF is interpolated by the Gaussian RBFs positioned at a predefined set of knots in the design domain. The Gaussian RBF is one of the typical GSRBFs, which has a higher level of interpolation accuracy and smoothness when comparing with other RBFs, such as CSRBFs [38,39]. The Gaussian RBFs ϕ_i are expressed as:

$$\varphi_i(\mathbf{x}) = \mathrm{e}^{-sr_i(\mathbf{x})^2} \quad (i=1,2,\ldots,N) \tag{10}$$

where r defined in a Euclidean space can be stated by

$$r_i(\mathbf{x}) = \|\mathbf{x}-\mathbf{x}_i\| \tag{11}$$

where $\mathbf{x}_i$ is the coordinate of knot i in domain D. $\|\mathbf{x}-\mathbf{x}_i\|$ is defined as the Euclidean norm that measures the distance from the current sample knot $\mathbf{x}$ to the knot $\mathbf{x}_i$ [38]. N is the total number of the interpolant knots, i.e. the level set knots in this study. s is the shape parameter that is assumed to be a positive constant [38]. In this study, s is equal to the reciprocal of the area (or volume) of a level set grid.

Using the Gaussian RBFs, the LSF is approximated by:

$$\Phi(\mathbf{x},t) = \varphi(\mathbf{x})\alpha(t) = \sum_{i=1}^{N}\varphi_i(\mathbf{x})\cdot\alpha_i(t) \tag{12}$$

where $\boldsymbol{\alpha}(t)=[\alpha_1(t),\alpha_2(t),\ldots,\alpha_N(t)]^T$ are the expansion coefficients in the RBF interpolation. $\boldsymbol{\phi}(\mathbf{x})=[\phi_1(\mathbf{x}),\phi_2(\mathbf{x}),\ldots,\phi_N(\mathbf{x})]$ contain all the RBFs. It is seen that the RBFs are space-dependent and the expansion coefficients are time-dependent. It is noticed that the Gaussian RBF uses all the interpolation knots in the design domain to calculate the LSF value at each sample knot, and thus can produce a very high interpolation accuracy [38]. However, its full interpolation matrix will cause a remarkable computation burden during optimization. Using a matrix form, Eq. (12) can be rewritten as:

$$\Phi = \mathbf{A}\alpha, \text{where}\Phi = \left[\Phi(\mathbf{x}_1,t),\Phi(\mathbf{x}_2,t),\ldots,\Phi(\mathbf{x}_N,t)\right]^T \tag{13}$$

$$\mathbf{A} = \begin{bmatrix}\varphi(\mathbf{x}_1)\\ \varphi(\mathbf{x}_2)\\ \ldots\\ \varphi(\mathbf{x}_N)\end{bmatrix} = \begin{bmatrix}\varphi_1(\mathbf{x}_1) & \varphi_2(\mathbf{x}_1) & \ldots & \varphi_N(\mathbf{x}_1)\\ \varphi_1(\mathbf{x}_2) & \varphi_2(\mathbf{x}_2) & \ldots & \varphi_N(\mathbf{x}_2)\\ \ldots & \ldots & \ldots & \ldots\\ \varphi_1(\mathbf{x}_N) & \varphi_2(\mathbf{x}_N) & \ldots & \varphi_N(\mathbf{x}_N)\end{bmatrix} \tag{14}$$

Matrix $\mathbf{A}$ is invertible. The sparsity of $\mathbf{A}$ significantly influences the efficiency of the proposed method.

Substituting Eq. (12) into the H-J PDE [19], it yields a system of ordinary differential equations (ODEs):

$$\varphi(\mathbf{x})\frac{\partial\alpha(t)}{\partial t} - \vartheta_{\mathrm{n}}|\nabla(\varphi(\mathbf{x})\alpha(t))| = 0, \alpha(t=0) = \alpha_0 \tag{15}$$

where $\boldsymbol{\alpha}_0$ is the expansion coefficient vector at t=0, which is obtained by solving (13) with the initial level set function. Then the normal velocity field ϑ_{n} is given by:

$$\vartheta_{\mathrm{n}} = \frac{\varphi(\mathbf{x})\alpha'(t)}{|\nabla(\varphi(\mathbf{x})\alpha(t))|}, \text{where}\alpha'(t) = \frac{\partial\alpha(t)}{\partial t} \tag{16}$$

Here, ϑ_{n} is computed by using all the interpolation knots over the design domain. It indicates that ϑ_{n} has been naturally extended to the entire domain, and thus it is unnecessary to introduce any extra velocity extension

schemes [17]. Since that the H-J PDEs have been transformed into a system of ODEs, the evolution of the LSF will be free of the CFL condition [18]. The topological shape optimization is finally changed to a generalized "size" optimization, to efficiently update the expansion coefficients $\alpha_i(t)$ via the gradient-based optimization algorithms [13,30].

2.2 DWT-based interpolation matrix compression

In the iPLSM, the DWT [40,41] is a key to alleviating the computational cost caused by the full interpolation matrix. It converts the original interpolation matrix $\mathbf{A}$ in Eq. (13) into its wavelet form $\bar{\mathbf{A}}$ with the same size. The matrix $\bar{\mathbf{A}}$ with wavelet basis can easily distinguish its essential and redundant elements. Thus, a thresholding scheme is then utilized to sweep out a proper number of useless elements in $\bar{\mathbf{A}}$, and reformulate a much sparser interpolation matrix $\widetilde{\mathbf{A}}_s$. Finally, the LSF in Eq. (13) can be efficiently evaluated by using the sparse matrix $\widetilde{\mathbf{A}}_s$.

Here, the classic one-level DWT with the Haar wavelets is employed [58], since it can produce adequate numerical accuracy and interpolation efficiency in regards to the topological shape optimizations. In Eq. (13), the vector $\boldsymbol{\alpha}$ with length N can be transformed into its wavelet basis by a pyramidal scheme [58]:

$$\alpha_k^{(1)} = h_1\alpha_{2k-1}^{(0)} + h_2\alpha_{2k}^{(0)}; d_k^{(1)} = g_1\alpha_{2k-1}^{(0)} + g_2\alpha_{2k}^{(0)} \tag{17}$$

where $\alpha^{(0)}$ denote the components in the original vector $\boldsymbol{\alpha}$. $\alpha_k^{(1)}$ and $d_k^{(1)}$ are the elements in a new vector $\bar{\alpha} = \left[\alpha_1^{(1)}, \alpha_2^{(1)}, ..., \alpha_{N/2}^{(1)}, d_1^{(1)}, d_2^{(1)}, ..., d_{N/2}^{(1)}\right]^T$ obtained by using the DWT, with ~~k~~ k = 1, 2, ..., N/2. It is noted that the length N must be an even number to complete the one-level DWT with the intact wavelet orders [58]. If N is odd, an easy way to tackle this issue is to add one extra term "0" in the original vector $\boldsymbol{\alpha}$ during the transformation process, and then remove the term "0" when recovering the original vector. $[h_1, h_2]$ = $\left[\sqrt{2}/2, \sqrt{2}/2\right]$ is the high pass filter, and $[g_1, g_2]$ = $\left[-\sqrt{2}/2, \sqrt{2}/2\right]$ is the low pass filter. For simplicity, a convolution matrix $\mathbf{W}$ with dimension ~~N~~ N × N is used to describe the pyramidal scheme [41]:

$$\mathbf{W} = \begin{bmatrix} h_1 h_2 0000\cdots0000 \\ 00 h_1 h_2 00\cdots0000 \\ \vdots\ddots\vdots \\ 000000\cdots h_1 h_2 00 \\ 000000\cdots00 h_1 h_2 \\ g_1 g_2 0000\cdots0000 \\ 00 g_1 g_2 00\cdots0000 \\ \vdots\ddots\vdots \\ 000000\cdots g_1 g_2 00 \\ 000000\cdots00 g_1 g_2 \end{bmatrix}_{N\times N} \tag{18}$$

Using the orthogonal matrix $\mathbf{W}$, the level set function $\bar{\Phi}$, expansion coefficient $\bar{\alpha}$ and interpolation matrix $\bar{\mathbf{A}}$ after transformation can be respectively obtained by:

$$\bar{\Phi} = \mathbf{W}\Phi and \bar{\alpha} = \mathbf{W}\alpha \tag{19}$$

$$\bar{\mathbf{A}} = \mathbf{W}\mathbf{A}\mathbf{W}^T \tag{20}$$

With the pre-multiplication of $\mathbf{W}$ on both sides of (13), the interpolation process can be reformulated as:

$$\mathbf{W}\Phi = \mathbf{W}\mathbf{A}\left(\mathbf{W}^T\mathbf{W}\right)\alpha \tag{21}$$

where the product of $\mathbf{W}^T$ and $\mathbf{W}$ yields a unit matrix.

Comparing the terms in Eqs. (19)–(21), one can obtain a new system of interpolation:

$$\bar{\Phi} = \bar{\mathbf{A}}\bar{\alpha} \tag{22}$$

Further, a sparse form of $\bar{\mathbf{A}}$, i.e. $\widetilde{\mathbf{A}}_s$, can be created by using the following threshold scheme [40]:

$$threshold(q) = \begin{cases} q, |q| \geq \kappa\bar{q}; \\ 0, otherwise. \end{cases} \tag{23}$$

where q denotes an arbitrary element in $\bar{\mathbf{A}}$, and $\bar{q}$ is the averaging absolute value of all elements in $\bar{\mathbf{A}}$. κ is a parameter to adjust the threshold. Now, a sparse form of (22) can be reformulated as:

$$\bar{\Phi} \approx \widetilde{\mathbf{A}}_s\bar{\alpha} \tag{24}$$

We assume that the predefined LSF at t = 0 is $\boldsymbol{\Phi}_0$ and its wavelet form is $\bar{\Phi}_0$. At the first iteration, the initial $\boldsymbol{\alpha}_0$ defined in Eq. (15) is obtained by a reverse process $\alpha_0 = \mathbf{W}^{-1}\bar{\alpha}_0$, where $\bar{\alpha}_0$ is the wavelet form of $\boldsymbol{\alpha}_0$. Here $\bar{\alpha}_0$ is

approximately solved by $\tilde{\alpha}_0 \approx \widetilde{\mathbf{A}}_s^{-1}\bar{\Phi}_0$. At the following iterations, the design variable $\boldsymbol{\alpha}$ is updated by a gradient-based optimization algorithm, and then $\tilde{\alpha}$ is obtained by Eq. (19). Finally, we update $\bar{\Phi}$ by Eq. (24), and obtain the LSF by a reconstruction process $\Phi = \mathbf{W}^{-1}\bar{\Phi}$.

As above, the matrix compression technique has been incorporated into the Gaussian RBF based parametric formulation to form a new iPLSM, which has low computational costs, while significantly improves the performance of the optimized design comparing to the conventional PLSM. Note that $\widetilde{\mathbf{A}}_s$ is calculated once and for all. Therefore, it is seen that the iPLSM only adds one extra transformation $\tilde{\alpha} = \mathbf{W}\alpha$ and one extra reconstruction $\Phi = \mathbf{W}^{-1}\bar{\Phi}$ at each iteration. Both the transformation and reconstruction use an extremely sparse system, whose computer cost is almost negligible.

3 Frequency response topology optimization

3.1 Minimizing local frequency response

Considering a structure with the harmonic load at the excitation frequency ω, the dynamic load and complex displacement are respectively represented as $\mathbf{p} = \mathbf{p}_{mag}e^{j\omega T_H}$, $\mathbf{u} = \mathbf{u}_{mag}e^{j\omega T_H}$. $\mathbf{p}_{mag}$ and $\mathbf{u}_{mag}$ denote the magnitude of the external force and the displacement field. j is the imaginary unit. Here, T_H denotes the time that is related to the harmonic functions rather than the level set functions. The topology optimization for minimizing frequency responses on some given parts of a structure can be given by:

$$\begin{aligned} &\underset{\alpha_i(i=1,\ldots,N)}{Minimize} : J_l(\boldsymbol{u}(\mathbf{x},\alpha)) = \int_{\omega_s}^{\omega_e} \left|\boldsymbol{u}_r^T \boldsymbol{u}_r\right| d\omega \\ &Subjectto : k(\boldsymbol{u},\boldsymbol{v}) + j\omega c(\boldsymbol{u},\boldsymbol{v}) - \omega^2 m(\boldsymbol{u},\boldsymbol{v}) = l(\boldsymbol{v}), \forall \boldsymbol{v} \in U \\ &U = \left\{\boldsymbol{u} : u_i \in H^1(\Omega), \boldsymbol{u} = 0 \text{on} \Gamma_D\right\} \\ &G(\mathbf{x},\alpha) = \int_\Omega dV - V_{\max} \le 0 \\ &\alpha_{\min} \le \alpha_i \le \alpha_{\max} \end{aligned} \tag{25}$$

where α_i (i=1,...,N) are the design variables (i.e. the expansion coefficients of RBF interpolation). α_{max} and α_{min} are the upper and lower bounds of α_i to stabilize the iteration [35], which will be further discussed in Section 4.3. J_l is the objective to measure the local frequency response [54,59], where $|\bullet|$ calculates the magnitude of a complex number. $\boldsymbol{u}_r$ indicate the displacements of the structural part r where the dynamic responses are to be optimized. [ω_s, ω_e] is the excitation frequency range. G is the volume constraint, and V_{max} is the maximum allowable volume of materials. U represents the kinematically admissible displacement field. For simplicity, in this study, the level set grid is assumed to be identical with the FE mesh. Thus, u_i is the displacement of an arbitrary FE (or level set) knot i in domain D. $H^1(\Omega)$ is the first Sobolev function space.

Note that $\boldsymbol{v}$ in (25) is the complex conjugate of the virtual displacement [59]. $k(\mathbf{u}, \mathbf{v})$ is the strain energy sesquilinear form, $m(\mathbf{u}, \mathbf{v})$ is mass sesquilinear form and $l(\mathbf{v})$ is the load semilinear form. Mathematically, the sesquilinear form is linear on the real displacement field but conjugate linear on the virtual displacement field, and the semilinear form is conjugate linear on the virtual displacement field [60]. Thus, following a similar way to Shu and co-workers [55,59,60], the following weak forms can be defined:

$$k(\mathbf{u},\mathbf{v}) = \int_\Omega E_{pqrs}\varepsilon_{pq}(\mathbf{u})\varepsilon_{rs}(\mathbf{v})dV \tag{26}$$

$$m(\mathbf{u},\mathbf{v}) = \int_\Omega \rho \mathbf{u}\mathbf{v} dV \tag{27}$$

$$l(\mathbf{v}) = \int_{\Gamma_N} \mathbf{p}\mathbf{v} dS \tag{28}$$

where E_{pqrs} is the elasticity tensor, ε is the structural strain, and ρ is the material density. $\mathbf{p}$ is the boundary traction (harmonic load), and dS indicates a boundary integral. The body force is not considered here. According to the Rayleigh damping assumption, the damping functional in (25) is calculated by the linear combination of the strain energy and mass sesquilinear forms with constants β_1 and β_2 [61]:

$$c(\mathbf{u},\mathbf{v}) = \beta_1 k(\mathbf{u},\mathbf{v}) + \beta_2 m(\mathbf{u},\mathbf{v}) \tag{29}$$

The integrals on objective J_l, which is used to evaluate the frequency response within a given excitation range, can be approximately calculated by different approaches [54,62]. Here, for simplicity, the numerical integration scheme with equally spaced abscissas [54] is adopted. We denote the local frequency response at a specified excitation frequency $\omega_z \in [\omega_s, \omega_e]$ as:

$$J_l^{\omega_z}(\mathbf{u}), where \omega_z = \omega_s + z\cdot\left(\omega_e - \omega_s\right)/NF \tag{30}$$

$$NF = \left(\omega_e - \omega_s\right)/\Delta\omega \tag{31}$$

where $\Delta\omega$ is the frequency interval, and NF denotes the number of frequencies included in evaluating the integral over the given excitation range. z=1,2,...,NF, which is the subscript to indicate the current frequency. Then the

objective function can be approximately calculated by:

$$J_l(\mathbf{u}) \approx \frac{\Delta\omega}{2}\cdot J_l^{\omega_1}(\mathbf{u}) + \sum_{z=2}^{NF-1}\Delta\omega\cdot J_l^{\omega_z}(\mathbf{u}) + \frac{\Delta\omega}{2}\cdot J_l^{\omega_{NF}}(\mathbf{u}) \tag{32}$$

3.2 Minimizing dynamic compliance

The topology optimization model for minimizing the global frequency response is formulated as:

$$\begin{aligned} \underset{\alpha_i(i=1,\ldots,N)}{Minimize}\ &: J_g(\boldsymbol{u}(\mathbf{x},\alpha)) = \int_{\omega_s}^{\omega_e}\left|\int_\Omega \boldsymbol{p}\boldsymbol{u}dV\right|d\omega \\ Subjecto\ &: k(\boldsymbol{u},\boldsymbol{v}) + j\omega c(\boldsymbol{u},\boldsymbol{v}) - \omega^2 m(\boldsymbol{u},\boldsymbol{v}) = l(\boldsymbol{v}), \forall \boldsymbol{v}\in U \\ &U = \left\{\boldsymbol{u} : u_i \in H^1(\Omega), \boldsymbol{u} = 0 \text{on}\Gamma_D\right\} \\ &G(\mathbf{x},\alpha) = \int_\Omega dV - V_{\max} \le 0 \\ &\alpha_{\min} \le \alpha_i \le \alpha_{\max} \end{aligned} \tag{33}$$

This model is similar to (25). However, its objective function J_g aims to optimize the dynamic compliance [47,54], so as to enhance the capability of resisting vibration over the whole structure. Note that the outer integral on J_g is also calculated by a similar scheme given in (32).

4 Sensitivity analysis and optimization algorithm

4.1 Design sensitivity analysis for minimizing local frequency response

Based on Eq. (32), it can be seen that the objective J_l is evaluated by $J_l^{\omega_z}$. Thus, it is essential to derive the sensitivity information for $J_l^{\omega_z}$:

$$J_l^{\omega_z} = \left|\mathbf{u}_r^T\mathbf{u}_r\right| = |J_u| = \sqrt{\left(real\left(J_u\right)\right)^2 + \left(imag\left(J_u\right)\right)^2} \tag{34}$$

where J_u is introduced to denote $\mathbf{u}_r^T\mathbf{u}_r$. $real(\bullet)$ and $imag(\bullet)$ respectively acquire the real and imaginary parts of a functional. According to Ref. [59], the design sensitivity of $J_l^{\omega_z}$ is derived by:

$$\frac{\partial J_l^{\omega_z}}{\partial\alpha_i} = \left(real\left(J_u\right)\cdot real\left(\frac{\partial J_u}{\partial\alpha_i}\right) + imag\left(J_u\right)\cdot imag\left(\frac{\partial J_u}{\partial\alpha_i}\right)\right) / \sqrt{\left(real\left(J_u\right)\right)^2 + \left(imag\left(J_u\right)\right)^2} \tag{35}$$

In Eq. (35), J_u can be obtained by FEM. Thus, we can now focus on the calculation of $\partial J_u/\partial\alpha_i$. To this end, we firstly present the derivative $\partial J_u/\partial t$:

$$\frac{\partial J_u}{\partial t} = \sum_{i=1}^{N}\frac{\partial J_u}{\partial\alpha_i(t)}\alpha'_i(t) = 2\mathbf{u}_r^T\mathbf{u}'_r \tag{36}$$

where $\mathbf{u}'_r$ denotes the derivative of $\mathbf{u}_r$ with respect to t.

The shape derivative [60,63] of the state equation in Eq. (25) can be derived as:

$$\begin{aligned} &\left(1+j\omega\beta_1\right)\left[k\left(\boldsymbol{u}',\boldsymbol{v}\right) + k\left(\boldsymbol{u},\boldsymbol{v}'\right) + \int_\Gamma E_{pqrs}\epsilon_{pq}(\mathbf{u})\epsilon_{rs}(\mathbf{v})\vartheta_{\mathrm{n}}dS\right] \\ &\quad + \left(j\omega\beta_2 - \omega^2\right)\left[m\left(\boldsymbol{u}',\boldsymbol{v}\right) + m\left(\boldsymbol{u},\boldsymbol{v}'\right) + \int_\Gamma \rho\mathbf{u}\mathbf{v}\vartheta_{\mathrm{n}}dS\right] \\ &\quad = \int_{\Gamma_N}\boldsymbol{p}\boldsymbol{v}'dS + \int_{\Gamma_N}\left(\nabla(\boldsymbol{p}\boldsymbol{v})\cdot\mathbf{n} + (\nabla\cdot\mathbf{n})\cdot(\boldsymbol{p}\boldsymbol{v})\right)\vartheta_{\mathrm{n}}dS \end{aligned} \tag{37}$$

where $\mathbf{u}'$ and $\mathbf{v}'$ represent the derivatives of $\mathbf{u}$ and $\mathbf{v}$ with respect to t. $\mathbf{n}$ is the outward normal vector along the boundary of Ω [19,20].

Considering that $\mathbf{v}'\in U$, we have the following vibrational state equation:

$$\left(1+j\omega\beta_1\right)k\left(\boldsymbol{u},\boldsymbol{v}'\right) + \left(j\omega\beta_2 - \omega^2\right)m\left(\boldsymbol{u},\boldsymbol{v}'\right) = \int_{\Gamma_N}\boldsymbol{p}\boldsymbol{v}'dS \tag{38}$$

Substituting Eq. (38) into Eq. (37), it yields:

$$\left(1+j\omega\beta_1\right)k\left(\boldsymbol{u}',\boldsymbol{v}\right)+\left(j\omega\beta_2-\omega^2\right)m\left(\boldsymbol{u}',\boldsymbol{v}\right)=\int_{\Gamma_N}\left(\nabla\left(\boldsymbol{pv}\right)\cdot\mathbf{n}+\left(\nabla\cdot\mathbf{n}\right)\cdot\left(\boldsymbol{pv}\right)\right)\vartheta_{\mathrm{n}}dS$$
$$-\int_{\Gamma}\left(\left(1+j\omega\beta_1\right)E_{pqrs}\varepsilon_{pq}\left(\boldsymbol{u}\right)\varepsilon_{rs}\left(\boldsymbol{v}\right)+\left(j\omega\beta_2-\omega^2\right)\rho\mathbf{uv}\right)\vartheta_{\mathrm{n}}dS \tag{39}$$

The local frequency response optimization is typically a non-self adjoint problem, and thus the adjoint variable method [60] is introduced to avoid the direct calculation of $\mathbf{u}'$. Considering the terms in (36), the following equation can be derived from (39) by replacing $\mathbf{v}$ with the adjoint variable $\mathbf{w}$:

$$2\mathbf{u}_r^T\mathbf{u}'_r=\int_{\Gamma_N}\left(\nabla\left(\mathbf{pw}\right)\cdot\mathbf{n}+\left(\nabla\cdot\mathbf{n}\right)\cdot\left(\mathbf{pw}\right)\right)\vartheta_{\mathrm{n}}dS$$
$$-\int_{\Gamma}\left(\left(1+j\omega\beta_1\right)E_{pqrs}\varepsilon_{pq}\left(\mathbf{u}\right)\varepsilon_{rs}\left(\mathbf{w}\right)+\left(j\omega\beta_2-\omega^2\right)\rho\mathbf{uw}\right)\vartheta_{\mathrm{n}}dS \tag{40}$$

where $\mathbf{w}$ is equal to the complex conjugate of variable $\mathbf{w}^*$ [60]. $\mathbf{w}^*$ can be obtained by solving the adjoint Eq. (41), which has the same sesquilinear form of the state equation in Eq. (25):

$$k\left(\bar{\mathbf{w}},\mathbf{w}^*\right)+j\omega c\left(\bar{\mathbf{w}},\mathbf{w}^*\right)-\omega^2 m\left(\bar{\mathbf{w}},\mathbf{w}^*\right)=l_a\left(\bar{\mathbf{w}}\right),\forall\bar{\mathbf{w}}\in U \tag{41}$$

where $\bar{\mathbf{w}}$ is the virtual adjoint variable, and $l_a\left(\bar{\mathbf{w}}\right)=2\mathbf{u}_r^T$ is regarded as the adjoint load term [55,60].

Comparing the terms in (36) and (40), the shape derivative of J_u is obtained by:

$$\frac{\partial J_u}{\partial t}=-\int_{\Gamma}\left(\left(1+j\omega\beta_1\right)E_{pqrs}\varepsilon_{pq}\left(\mathbf{u}\right)\varepsilon_{rs}\left(\mathbf{w}\right)+\left(j\omega\beta_2-\omega^2\right)\rho\mathbf{uw}\right)\vartheta_{\mathrm{n}}dS \tag{42}$$

It should be noted that Γ_N is assumed to be fixed while (42) is being derived, and thus the integral over Γ_N vanishes. Substituting ϑ_{n} defined in (16) into (42), it yields:

$$\frac{\partial J_u}{\partial t}=-\int_{\Gamma}\left(\left(1+j\omega\beta_1\right)E_{pqrs}\varepsilon_{pq}\left(\mathbf{u}\right)\varepsilon_{rs}\left(\mathbf{w}\right)+\left(j\omega\beta_2-\omega^2\right)\rho\mathbf{uw}\right)\frac{\varphi\left(\mathbf{x}\right)\alpha'\left(t\right)}{\left|\nabla\left(\varphi\left(\mathbf{x}\right)\alpha\left(t\right)\right)\right|}dS \tag{43}$$

When introducing the Dirac delta function given in (7), we can have following mapping relation [21]:

$$\int_{\Gamma}dS=\int_{D}\widetilde{\delta}\left(\Phi\right)\left|\nabla\Phi\right|dV \tag{44}$$

To facilitate the implementation, Eq. (43) can be reformulated as a volume integral via Eq. (44) [36]:

$$\frac{\partial J_u}{\partial t}=-\int_{D}\left(\left(1+j\omega\beta_1\right)E_{pqrs}\varepsilon_{pq}\left(\mathbf{u}\right)\varepsilon_{rs}\left(\mathbf{w}\right)+\left(j\omega\beta_2-\omega^2\right)\rho\mathbf{uw}\right)\widetilde{\delta}\left(\Phi\right)\varphi\left(\mathbf{x}\right)\alpha'\left(t\right)dV$$
$$=-\sum_{i=1}^{N}\int_{D}\left(\left(1+j\omega\beta_1\right)E_{pqrs}\varepsilon_{pq}\left(\mathbf{u}\right)\varepsilon_{rs}\left(\mathbf{w}\right)+\left(j\omega\beta_2-\omega^2\right)\rho\mathbf{uw}\right)\widetilde{\delta}\left(\Phi\right)\varphi_i\left(\mathbf{x}\right)\alpha'_i\left(t\right)dV \tag{45}$$

Comparing the corresponding terms in (36) and (45), and eliminating $\alpha'_i(t)$, it yields:

$$\frac{\partial J_u}{\partial\alpha_i}=-\int_{D}\left(\left(1+j\omega\beta_1\right)E_{pqrs}\varepsilon_{pq}\left(\mathbf{u}\right)\varepsilon_{rs}\left(\mathbf{w}\right)+\left(j\omega\beta_2-\omega^2\right)\rho\mathbf{uw}\right)\widetilde{\delta}\left(\Phi\right)\varphi_i\left(\mathbf{x}\right)dV \tag{46}$$

Eq. (46) can be calculated numerically according to Eq. (9). However, it is remarked that the element-wise quantities in (9) should be extended to the FE nodes via shape functions [31], because that the RBFs $\phi_i(\mathbf{x})$ are defined at each node. By virtue of $\partial J_u/\partial\alpha_i$, it is easy to calculate the sensitivity $\partial J_l^{\omega_z}/\partial\alpha_i$ at a single frequency ω_z corresponding to Eq. (35). With $\partial J_l^{\omega_z}/\partial\alpha_i$, the sensitivity of the objective function $\partial J_l/\partial\alpha_i$ can be evaluated using a similar integration scheme given in (32).

Similarly, the sensitivity of the volume constraint can be derived as:

$$\frac{\partial G}{\partial\alpha_i}=\int_{D}\widetilde{\delta}\left(\Phi\right)\varphi_i\left(\mathbf{x}\right)dV \tag{47}$$

4.2 Design sensitivity analysis for minimizing dynamic compliance

Assuming $J_g^{\omega_z}$ is the dynamic compliance at a frequency $\omega_z\in[\omega_s,\omega_e]$, the objective J_g can be evaluated by $J_g^{\omega_z}$ at each integration point by using a similar scheme defined in (32). Thus, it is important to obtain the sensitivity information for $J_g^{\omega_z}$:

$$J_g^{\omega_z} = \left| \int_\Omega \mathbf{p}\mathbf{u} dV \right| = |J_d| = \sqrt{\left(real\left(J_d\right)\right)^2 + \left(imag\left(J_d\right)\right)^2} \tag{48}$$

where J_d is introduced to denote $\int_\Omega \boldsymbol{pu} dV$. The design sensitivity of $J_g^{\omega_z}$ is then given by:

$$\frac{\partial J_g^{\omega_z}}{\partial \alpha_i} = \left(real\left(J_d\right) \cdot real\left(\frac{\partial J_d}{\partial \alpha_i}\right) + imag\left(J_d\right) \cdot imag\left(\frac{\partial J_d}{\partial \alpha_i}\right) \right) / \sqrt{\left(real\left(J_d\right)\right)^2 + \left(imag\left(J_d\right)\right)^2} \tag{49}$$

J_d is obtained by FEM, and we now focus on the calculation of $\partial J_d / \partial \alpha_i$. Here, J_d is re-written by:

$$\begin{aligned} J_d &= \int_\Omega \left(1 + j\omega\beta_1\right) E_{pqrs} \varepsilon_{pq}\left(\boldsymbol{u}\right) \varepsilon_{rs}\left(\boldsymbol{u}\right) dV + \int_\Omega \left(j\omega\beta_2 - \omega^2\right) \rho \mathbf{u}\mathbf{u} dV \\ &= \left(1 + j\omega\beta_1\right) k\left(\boldsymbol{u}, \boldsymbol{u}\right) + \left(j\omega\beta_2 - \omega^2\right) m\left(\boldsymbol{u}, \boldsymbol{u}\right) \end{aligned} \tag{50}$$

The shape derivative of J_d can be derived by:

$$\begin{aligned} \frac{\partial J_d}{\partial t} &= 2\left(1 + j\omega\beta_1\right) k\left(\boldsymbol{u}', \boldsymbol{u}\right) + 2\left(j\omega\beta_2 - \omega^2\right) m\left(\boldsymbol{u}', \boldsymbol{u}\right) \\ &+ \int_\Gamma \left(\left(1 + j\omega\beta_1\right) E_{pqrs} \varepsilon_{pq}\left(\boldsymbol{u}\right) \varepsilon_{rs}\left(\boldsymbol{u}\right) + \left(j\omega\beta_2 - \omega^2\right) \rho \mathbf{u}\mathbf{u} \right) \vartheta_{\mathrm{n}} dS \end{aligned} \tag{51}$$

Since that the state equations for the global and local frequency response optimizations are similar, Eq. (39) is also applicable to this problem. Considering that dynamic compliance minimization is self-adjoint, Eq. (39) can be rewritten by:

$$\begin{aligned} \left(1 + j\omega\beta_1\right) k\left(\boldsymbol{u}', \boldsymbol{u}\right) + \left(j\omega\beta_2 - \omega^2\right) m\left(\boldsymbol{u}', \boldsymbol{u}\right) &= \int_{\Gamma_N} \left(\nabla\left(\boldsymbol{pu}\right) \cdot \mathbf{n} + \left(\nabla \cdot \mathbf{n}\right) \cdot \left(\boldsymbol{pu}\right)\right) \vartheta_{\mathrm{n}} dS \\ - \int_\Gamma \left(\left(1 + j\omega\beta_1\right) E_{pqrs} \varepsilon_{pq}\left(\boldsymbol{u}\right) \varepsilon_{rs}\left(\boldsymbol{u}\right) + \left(j\omega\beta_2 - \omega^2\right) \rho \mathbf{u}\mathbf{u} \right) \vartheta_{\mathrm{n}} dS \end{aligned} \tag{52}$$

Then the shape derivative of J_d can be obtained by substituting Eq. (52) into Eq. (51):

$$\frac{\partial J_d}{\partial t} = -\int_\Gamma \left(\left(1 + j\omega\beta_1\right) E_{pqrs} \varepsilon_{pq}\left(\boldsymbol{u}\right) \varepsilon_{rs}\left(\boldsymbol{u}\right) + \left(j\omega\beta_2 - \omega^2\right) \rho \mathbf{u}\mathbf{u} \right) \vartheta_{\mathrm{n}} dS \tag{53}$$

Note that Γ_N is fixed while (53) is being derived, and thus the integral over Γ_N is eliminated.

Similar to the process described by Eqs. (43)–(45), we can reformulate $\partial J_d / \partial t$ as:

$$\frac{\partial J_d}{\partial t} = -\sum_{i=1}^{N} \int_D \left(\left(1 + j\omega\beta_1\right) E_{pqrs} \varepsilon_{pq}\left(\mathbf{u}\right) \varepsilon_{rs}\left(\mathbf{u}\right) + \left(j\omega\beta_2 - \omega^2\right) \rho \mathbf{u}\mathbf{u} \right) \widetilde{\delta}\left(\Phi\right) \varphi_i\left(\mathbf{x}\right) \alpha'_i\left(t\right) dV \tag{54}$$

On the other hand, $\partial J_d / \partial t$ can be also derived by the chain rule:

$$\frac{\partial J_d}{\partial t} = \sum_{i=1}^{N} \frac{\partial J_d}{\partial \alpha_i\left(t\right)} \alpha'_i\left(t\right) \tag{55}$$

By comparing the corresponding terms in (54) and (55), $\partial J_d / \partial \alpha_i$ can be easily given by:

$$\frac{\partial J_d}{\partial \alpha_i} = -\int_D \left(\left(1 + j\omega\beta_1\right) E_{pqrs} \varepsilon_{pq}\left(\mathbf{u}\right) \varepsilon_{rs}\left(\mathbf{u}\right) + \left(j\omega\beta_2 - \omega^2\right) \rho \mathbf{u}\mathbf{u} \right) \widetilde{\delta}\left(\Phi\right) \varphi_i\left(\mathbf{x}\right) dV \tag{56}$$

Similarly, Eq. (56) can be calculated numerically according to Eq. (9), with all the element-wise quantities extending to the FE nodes. By virtue of $\partial J_d / \partial \alpha_i$, the sensitivity $\partial J_g^{\omega_z} / \partial \alpha_i$ can be computed via Eq. (49). With $\partial J_g^{\omega_z} / \partial \alpha_i$, the sensitivity of the objective function $\partial J_g / \partial \alpha_i$ can be calculated by a similar integration scheme defined in (32). The sensitivity of volume constraint is the same as (47).

4.3 Optimization algorithm

In the iPLSM, the expansion coefficients α_i in the RBF interpolation serve as the design variables, but it is unable to identify their fixed upper and lower bounds (i.e. $\alpha_{\max}$ and $\alpha_{\min}$) during optimization. However, it is able to specify the fixed bounds $\widetilde{\alpha}_{\min} \le \widetilde{\alpha}_i \le \widetilde{\alpha}_{\max}$ on the regularized design variables $\widetilde{\alpha}_i$. Hence, an OC-based optimization algorithm [10,13] can be established, as follows:

Step 1 Calculating the regularized design variables:

$$\widetilde{\alpha}_i^{(\xi)} = \frac{\alpha_i^{(\xi)} - \alpha_{\min}^{(\xi)}}{\alpha_{\max}^{(\xi)} - \alpha_{\min}^{(\xi)}}, where \alpha_{\max}^{(\xi)} = 2 \times \max\left(\alpha_i^{(\xi)}\right), \alpha_{\min}^{(\xi)} = 2 \times \min\left(\alpha_i^{(\xi)}\right) \quad (57)$$

where ξ indicates the current iteration number.

Step 2 Based on the Kuhn-Tucker conditions [10,13], the following heuristic scheme can be established to iteratively update the regularized design variables $\widetilde{\alpha}_i$:

$$\widetilde{\alpha}_i^{(\xi+1)} = \begin{cases} \min\left[\left(\widetilde{\alpha}_i^{(\xi)} + \sigma\right), \widetilde{\alpha}_{\max}\right], & if \min\left[\left(\widetilde{\alpha}_i^{(\xi)} + \sigma\right), \widetilde{\alpha}_{\max}\right] \le \left(B_i^{(\xi)}\right)^{\ell} \widetilde{\alpha}_i^{(\xi)} \\ \left(B_i^{(\xi)}\right)^{\ell} \widetilde{\alpha}_i^{(\xi)}, & if \begin{cases} \max\left[\left(\widetilde{\alpha}_i^{(\xi)} - \sigma\right), \widetilde{\alpha}_{\min}\right] < \left(B_i^{(\xi)}\right)^{\ell} \widetilde{\alpha}_i^{(\xi)} \\ \left(B_i^{(\xi)}\right)^{\ell} \widetilde{\alpha}_i^{(\xi)} < \min\left[\left(\widetilde{\alpha}_i^{(\xi)} + \sigma\right), \widetilde{\alpha}_{\max}\right] \end{cases} \\ \max\left[\left(\widetilde{\alpha}_i^{(\xi)} - \sigma\right), \widetilde{\alpha}_{\min}\right], & if \left(B_i^{(\xi)}\right)^{\ell} \widetilde{\alpha}_i^{(\xi)} \le \max\left[\left(\widetilde{\alpha}_i^{(\xi)} - \sigma\right), \widetilde{\alpha}_{\min}\right] \end{cases} \quad (58)$$

where the moving limit σ(0 < σ < 1) and damping factor ℓ(0 < ℓ < 1) are two parameters to stabilize the optimization [10,13]. Here, we have $\widetilde{\alpha}_{\max} = 1$ and $\widetilde{\alpha}_{\min} = 0.001$. As $\widetilde{\alpha}_i$ is obtained by a linear function (57) of α_i, $B_i^{(\xi)}$ can be given by:

$$B_i^{(\xi)} = -\frac{\partial J_l}{\partial \alpha_i^{(\xi)}} / \max\left(\mu, \Lambda^{(\xi)} \frac{\partial G}{\partial \alpha_i^{(\xi)}}\right) or -\frac{\partial J_g}{\partial \alpha_i^{(\xi)}} / \max\left(\mu, \Lambda^{(\xi)} \frac{\partial G}{\partial \alpha_i^{(\xi)}}\right) \quad (59)$$

where μ=1e-10 is used to avoid the zero terms. At each iteration, the Lagrange multipliers $\Lambda^{(\xi)}$ can be found by a bi-sectioning approach [10].

Step 3 Updating the design variables:

$$\alpha_i^{(\xi+1)} = \widetilde{\alpha}_i^{(\xi+1)} \times \left(\alpha_{\max}^{(\xi)} - \alpha_{\min}^{(\xi)}\right) + \alpha_{\min}^{(\xi)} \quad (60)$$

Step 4 Repeating ***Step 1*** to ***Step 3*** until a convergent criterion is reached.

5 Numerical implementations

5.1 Localized modes

In the most standard SIMP topology optimization [13,14], the element density ρ_h^{SIMP} and Young's modulus E_h^{SIMP} are interpolated by:

$$\rho_h^{SIMP} = \eta_h \rho, E_h^{SIMP} = \left(\eta_h\right)^p E \quad (61)$$

where η_h is the pseudo-density of element h, p is the penalty factor, and E is the Young's modulus for a solid element. While the element density ρ_h^{iPLSM} and Young's modulus E_h^{iPLSM} in iPLSM can be defined according to the ersatz material model given in Eq. (5):

$$\rho_h^{iPLSM} = \chi_h \rho, E_h^{iPLSM} = \chi_h E \quad (62)$$

The localized modes phenomenon [42,54,64,65] may appear in the SIMP-based methods. The reason is that the power-law in classic SIMP may lead to a big difference between the element mass and stiffness matrices when the density of weak material is close to its minimum value [65]. This difference is measured by the ratio of coefficients before ρ and E, i.e. $\eta_h/(\eta_h)^p$ [64,65]. The material interpolation curves of the SIMP method and iPLSM are shown in Fig. 2. In the ersatz material model, the ratio of coefficients before ρ and E in iPLSM is always equivalent to 1. In this case, the localized modes can be naturally avoided.

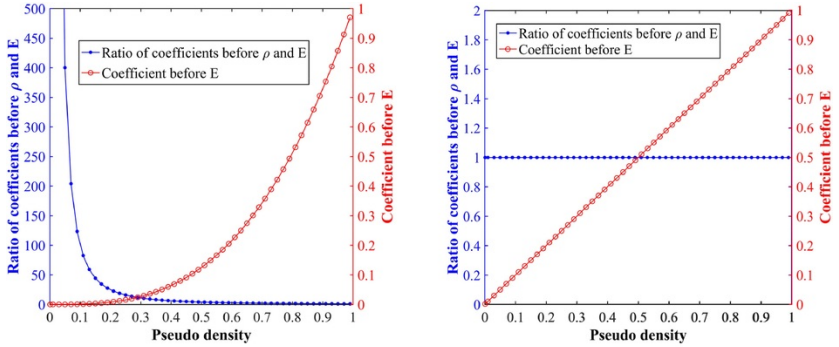

Fig. 2 Material interpolation curves: (a) classic SIMP method with p=3 and (b) iPLSM.

alt-text: Fig. 2.

5.2 Filtering scheme

In iPLSM, a filtering scheme is applied to the element pseudo-density χ_h at each iteration. On one hand, the filtering scheme will increase the smoothness of design sensitivities, because neither the smooth Heaviside function [19] nor the ersatz material model [20] can exactly describe the design boundary and the design sensitivities [35,66]. On the other hand, the filtering scheme is used to alleviate the mesh-dependency issue [67,68], by improving the continuity of the pseudo-density field.

The filter on element pseudo-density χ_h can be defined as:

$$\bar{\chi}_h = \sum_{h=1}^{NE}\left(\sum_{f=1}^{NH}\theta_{h,f}\chi_f / \sum_{f=1}^{NH}\theta_{h,f}\right), where \theta_{h,f} = \bar{\theta}_{h,f} / \sum_{f=1}^{NH}\bar{\theta}_{h,f} \tag{63}$$

$$\bar{\theta}_{h,f} = \sum_{h=1}^{NE}\left(\sum_{f=1}^{NH}\frac{3}{\pi r_{\min}^2}\max\left(0, \frac{r_{\min} - dist(h,f)}{r_{\min}}\right)\right) \tag{64}$$

where $\bar{\chi}_h$ is the filtered element pseudo-density. $\theta_{h,f}$ is the convolution defined by the radially linear hat function $\bar{\theta}_{h,f}$. NH is the number of finite elements (i.e. element f) located within the given filtering window of element h. $r_{\min}$ defines the radius of the filter area, which is typically 1.5 - 2.0 times of the mesh size. $dist(h, f)$ represents the distance between element h and f.

5.3 Model reduction scheme

In the frequency response optimization within a wide excitation frequency range, a considerable number of repetitive FE calls are implemented during each iteration. Model reduction (MR) schemes [48] can transform the stiffness matrix, damping matrix and mass matrix with highly refined mesh into smaller matrices via mapping their nodal coordinates to a reduced set of generalized or modal coordinates. Therefore, the MR schemes can be applied to FE analysis process to alleviate the expensive computer cost. In this paper, the widely-accepted quasi-static Ritz vector (QSRV) [48,54,57,69] is applied to approximate the structural frequency response with reasonable accuracy while reduce the computational cost. The readers can refer to Ma and co-workers [48,54,57,69] for more details about the well-established QSRV approach.

6 Numerical examples

This section provides several examples to show the features of the proposed method. In all examples, the solid material is selected as a type of steel, which has the Young's moduli 210 GPa, Poisson's ratio 0.3 and density ρ=7.8 g/cm^3. The structural damping coefficients are β_1=0.001 and β_2=0.03, respectively. It is easy to see from Eq. (32) that a smaller value of $\Delta\omega$ will include more integral points to compute the objectives and their sensitivities, which can produce higher accuracy but greater computational cost in approximating the integrals. On the contrary, larger $\Delta\omega$ will reduce the computational cost by sacrificing the numerical precision. According to the experiential criterion [54], $\Delta\omega$ can be selected from 1 Hz to 10 Hz by making a tradeoff between numerical accuracy and cost. Here, for simplicity, the frequency interval in Eqs. (31) and (32) for each example is fixed as $\Delta\omega$=10Hz, and the number of frequencies NF can be calculated by using Eq. (31) accordingly. To avoid early convergence, the objectives of the last few iterations are used to define the convergence criterion for the optimization. The relative difference of the objective functions between two successive steps at the current iteration ξ is denoted as $\Upsilon^{(\xi)}$. The iteration is terminated when $\Upsilon^{(\xi-2)}$, $\Upsilon^{(\xi-1)}$ and $\Upsilon^{(\xi)}$ are all less than 0.0005.

All the examples are implemented with MATLAB via the same desktop. To facilitate the discussion, we denote the conventional PLSM with CSRBF interpolation as PLSM-1, and the PLSM with Gaussian RBF interpolation as PLSM-2. Both the PLSM-1 and PLSM-2 are without the DWT scheme. When comparing different optimization methods (i.e. iPLSM, PLSM-1 and PLSM-2), all other optimization settings (including the initial designs) are always kept the same except their interpolation mechanisms.

6.1 Local frequency response optimization for excited point of 2D structure

A 2D beam is shown in Fig. 3, with the size of 140 ~~cm~~ cm ~~×~~ × 20 ~~cm~~ cm ~~×~~ × 1 cm. The left and right sides are fixed. A harmonic excitation force $1000e^{j\omega T}$ N is vertically loaded at the center. This example aims at minimizing the frequency response at the loaded point **P** with the excitation frequency range Ω_{freq} = [0 Hz, 100 Hz]. The maximum material usage is restricted to 40%.

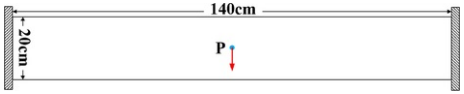

Fig. 3 Design domain of first example.

alt-text: Fig. 3.

Firstly, the structure is optimized by the iPLSM, with a thresholding factor κ=1 (see Eq. (23)). The structure is discretized with ~~280~~ 280 ~~×~~ × 40 four-node elements. Correspondingly, a set of Gaussian RBF knots (~~281~~ 281 ~~×~~ × 41 = 11,521) are used to interpolate the level set function, which produces a large interpolation matrix **A** (11,~~521~~ 521 ~~×~~ × 11,521). By virtue of the DWT scheme, the transformed matrix $\tilde{\mathbf{A}}_s$ is of the same size as matrix **A** but involves 99.74% zero elements. It implies remarkable reduction in both the computational cost and computer storage. Fig. 4 shows the structural topology and shape changes over iterations. An arbitrary initial design with holes is given in Fig. 4(a), with its material usage 54% and the fundamental eigenfrequency 191 Hz. As shown in Fig. 4(f), the optimized design is characterized with smooth boundary and distinct material interface, due to the level set boundary representation. During the optimization, the existing holes can be merged and new holes can be created to achieve the optimal design. Furthermore, the optimized design shows a similar but clearer boundary when compared to the result given in [48].

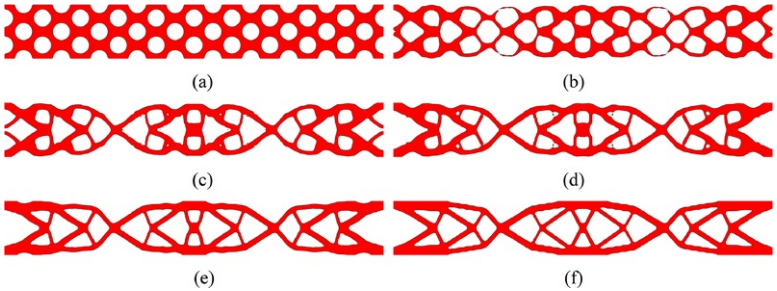

Fig. 4 Evolution of structural topology and shape: (a) initial design; (b) step 10; (c) step 15; (d) step 25; (e) step 50; (f) optimized design.

alt-text: Fig. 4.

The iterative history is shown in Fig. 5(a), and the frequency response functions (FRF) [54] of the initial and optimal designs are presented in Fig. 5(b). It takes 125 steps to converge, and the objective function is minimized gradually after the volume constraint is satisfied. The fundamental eigenfrequency of optimal design is increased to 343 Hz with only 40% material usage. The local frequency response of the optimal design is decreased remarkably from 4.5579e-~~-~~3 to 7.1168e-~~-~~4 (84% reduction) when comparing with the initial design, which confirms that the optimal design has an excellent performance in resisting the vibration at a specified point. The FRF curves also indicate a considerable reduction on local frequency response, as the area being comprised of the coordinate axis and FRF curve of the optimal design within the considered excitation frequency range is much smaller than that of the initial design.

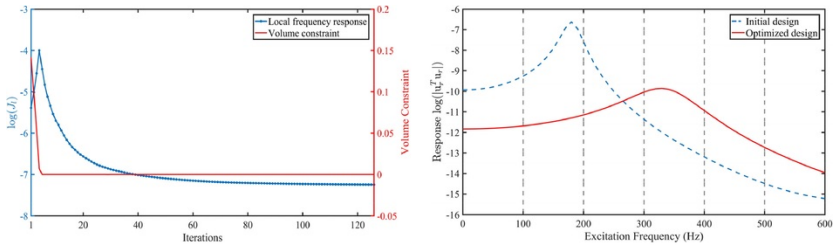

Fig. 5 Curves of first example using iPLSM with κ=1: (a) convergent histories of objective function and volume constraint; (b) FRF of excitation point before and after optimization.

alt-text: Fig. 5.

Secondly, the structure in Fig. 3 is optimized by the iPLSM with different thresholding factor κ. The initial designs as well as the optimization settings in different cases are exactly the same. As seen in Table 1, different κ have limited impact on the optimal results (similar objective values), but they indeed influence the computational costs. For instance, the processing time and computer storage are less for a larger κ (e.g. κ=1). Hence, in the following examples, κ=1 will be adopted.

Table 1 Investigation of iPLSM with different κ.

alt-text: Table 1

κ	Size of matrix **A**	Sparsity of matrix $\widetilde{\mathbf{A}}_s$	Time per step	Iterations	Objective
1e−500	11,521 × 11,521	64.27%	128.1 s	124	7.1202e−4
1e−300	11,521 × 11,521	86.13%	69.1 s	125	7.1170e−4
1e−200	11,521 × 11,521	89.94%	68.2 s	125	7.1169e−4
1	11,521 × 11,521	99.74%	65.3 s	125	7.1168e−4

In addition, the structure in Fig. 3 is optimized by using different FE meshes (or level set grids). For comparison, the optimal designs obtained by using the PLSM-1 [35], PLSM-2 and iPLSM are provided, respectively. The optimal topologies obtained by the iPLSM are plotted in Fig. 6, and the optimal results by using different optimization methods are given in Table 2. In Fig. 6, three designs are practically identical with the mesh refinements, owing to the filter scheme in the proposed method. It confirms that the iPLSM can alleviate the mesh-dependency in the optimization.

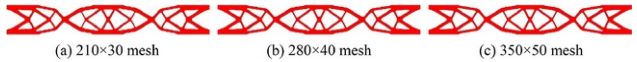

Fig. 6 Optimal topologies of first example with different meshes by using iPLSM.

alt-text: Fig. 6.

Table 2 Comparison of different methods in local frequency response optimization.

alt-text: Table 2

Method	Mesh	Size of matrix **A**	Sparsity of matrix **A** or $\widetilde{\mathbf{A}}_s$	Time per step	Iterations	Objective
iPLSM	210 × 30	6541 × 6541	99.54%	24.3 s	119	7.0187e−4
PLSM-1	210 × 30	6541 × 6541	99.18%	24.6 s	145	7.3016e−4
PLSM-2	210 × 30	6541 × 6541	0%	64.6 s	105	7.0443e−4
iPLSM	280 × 40	11,521 × 11,521	99.74%	65.3 s	125	7.1168e−4

PLSM-1	280×40	11,521	99.53%	65.9 s	161	7.3518e−4
PLSM-2	280×40	11,521	0%	197.2 s	127	7.1105e−4
iPLSM	350×50	17,901	99.83%	128.6 s	136	7.1280e−4
PLSM-1	350×50	17,901	99.69%	129.5 s	202	7.4264e−4
PLSM-2	350×50	17,901	0%	459.7 s	134	7.1344e−4

Apparently, as indicated in Table 2, the PLSM-1 always produces the worse objectives and requires more iterations when comparing to the other two methods. It is mainly because that the CSRBFs only measure the contributions of neighboring knots to a sample knot within a limited sub-region, which causes the accuracy loss in the interpolation. The accuracy loss prolongs the iterative process and eventually leads the optimization towards a worse local minimum. The PLSM-2 can achieve better objectives than the PLSM-1, with a prohibitive computation cost caused by the full interpolation matrix. The reason is that the Gaussian RBFs use all the interpolation knots to calculate the LSF value at each sample knot, and they require considerable computer efforts to guarantee a higher interpolation accuracy in approximating the topology and shape of the moving boundary. Thus, it is more likely to take fewer iterations to find an optimized design with higher performance.

Most importantly, the statistics in Table 2 demonstrate that the iPLSM is obviously more efficient than the other two methods. On one hand, the iPLSM can more rapidly find a higher-performance design when comparing to the PLSM-1. On the other hand, the iPLSM can remarkably reduce the computer storage and optimization time comparing with the PLSM-2. The reason lies in the fact that the iPLSM can well maintain the high interpolation accuracy of the GSRBF, while efficiently compress the full interpolation matrix by using the DWT.

6.2 Local frequency response optimization for multiple points of 2D structure

Here, the frequency response optimizations at both the excited and non-excited points are investigated. The design domain is shown in Fig. 7, with an excitation force $1000e^{j\omega T_H}$N vertically applying at point $\mathbf{P_1}$. In this example, the basic structure with the thickness 0.01 cm will be reinforced by an additional layer with 1 cm thickness. The objective is to minimize the structural frequency response at $\mathbf{P_1}$ and $\mathbf{P_2}$ with a reinforcement material usage of 40%. Four excitation frequency ranges are considered, e.g. [0 Hz, 100 Hz], [0 Hz, 200 Hz], [0 Hz, 400 Hz] and [400 Hz, 600 Hz]. The FE mesh is 280×40, and the initial holes within the design domain is the same as the first example.

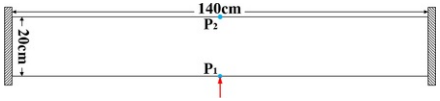

Fig. 7 Design domain of second example.

alt-text: Fig. 7.

The iPLSM is applied in all the cases. The optimal results are shown in Fig. 8, where the basic and reinforcement materials are marked with grey and red, respectively. The objective functions J_i of both the initial and optimal design for the four cases are also given in Fig. 8. Obviously, even though the magnitude of the external load remains unchanged, the optimized designs and objective functions are different under different excitation ranges. This is because that the optimization only minimizes the vibration within the concerned excitation frequency range, and it is not able to ensure a unique optimal design with regard to other excitation frequency ranges. Comparing with the first 3 cases, it can be seen that the design under wider excitation frequency range (i.e. Ω_{freq}=[0 Hz, 400 Hz]) has a greater objective function. The reason is that more integral points (i.e. frequency response at a single excitation frequency) are usually required in Eq. (32) to calculate the objective of the case with wider frequency range when the frequency interval is fixed as $\Delta\omega$=10Hz. Moreover, the design within Ω_{freq}=[400 Hz, 600 Hz] has the lowest objective among the 4 cases. It implies that higher frequency range (i.e. [400 Hz, 600 Hz]) may have a lower frequency response in this problem.

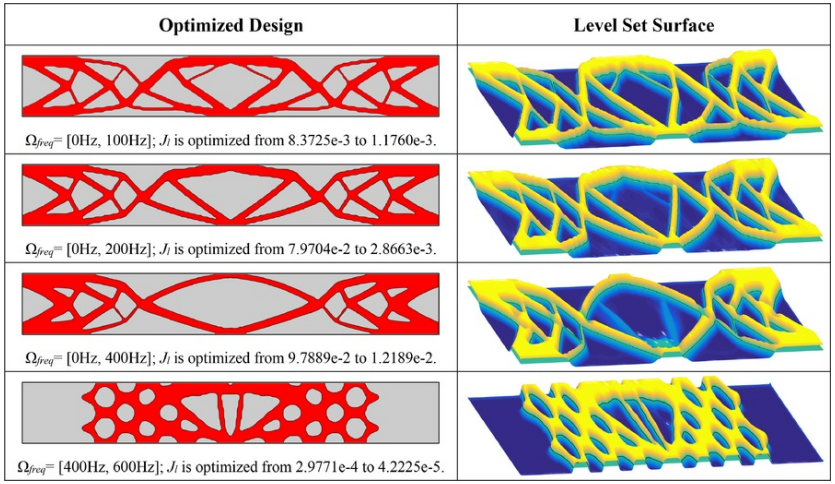

Fig. 8 Optimized designs of second example under different excitation frequency ranges.

alt-text: Fig. 8.

Table 3 presents the first 4 eigenfrequencies of the initial and optimized designs. The fundamental frequency of the initial designs is all 189 Hz, which are outside the frequency ranges [0 Hz, 100 Hz] and [400 Hz, 600 Hz] but within the ranges [0 Hz, 200 Hz] and [0 Hz, 400 Hz]. The FRF curves are given in Fig. 9. It can be seen that the resonance peaks of the optimized structures are moved to high frequencies for the first 3 cases but decreased to a low frequency for the last case. The fundamental eigenfrequency of each optimized design is moved outside the excitation frequency range to avoid resonance. In particular, when Ω_{freq} = [400 Hz, 600 Hz] is considered in this example, it is almost impossible to increase the fundamental frequency of the optimized structure up to 600 Hz. As a result, its fundamental eigenfrequency reduces to move outside [400 Hz, 600 Hz]. To this end, the optimized topology of the last case is significantly different from those of the first 3 cases, which only has base materials (without any reinforcement materials) on the two ends. A very similar observation can be found in [54]. By comparing the FRF curves of the initial and optimized designs, remarkable reductions on frequency responses of the optimized designs are observed. These confirm that the proposed method is effective in increasing the dynamic performance of a structure within the concerned excitation frequency range.

Table 3 Eigenfrequencies of initial design and optimized designs.

alt-text: Table 3

Eigenfrequency order	1st	2nd	3rd	4th
Initial design	189 Hz	484 Hz	739 Hz	869 Hz
Optimized design with Ω_{freq} = [0 Hz, 100 Hz]	342 Hz	564 Hz	853 Hz	1085 Hz
Optimized design with Ω_{freq} = [0 Hz, 200 Hz]	371 Hz	564 Hz	878 Hz	1085 Hz
Optimized design with Ω_{freq} = [0 Hz, 400 Hz]	438 Hz	577 Hz	1000 Hz	1141 Hz
Optimized design with Ω_{freq} = [400 Hz, 600 Hz]	91 Hz	203 Hz	210 Hz	717 Hz

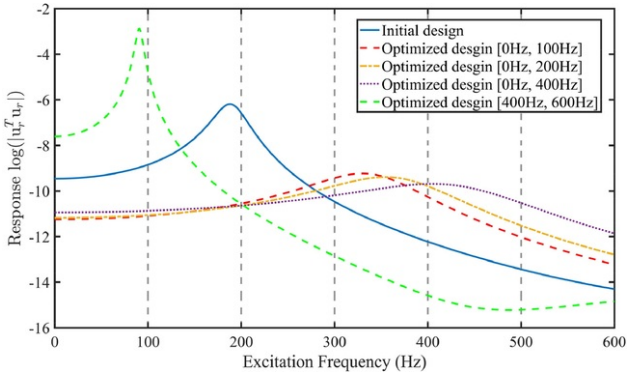

Fig. 9 FRF of points $\mathbf{P_1}$ and $\mathbf{P_2}$ before and after optimization. (For interpretation of the references to color in this figure legend, the reader is referred to the web version of this article.)

alt-text: Fig. 9.

6.3 Global frequency response optimization of 2D structure

Here, the objective is to minimize the dynamic compliance within the excitation frequency range Ω_{freq}=[0 Hz, 100 Hz]. A 2D cantilever beam (120 ~~cm~~ cm ~~×~~ × 60 ~~cm~~ cm ~~×~~ × 1 cm) is shown in Fig. 10, where an excitation force $100e^{j\omega T_n}$N is vertically applied at point **P**. The FE mesh is ~~120~~ 120 ~~×~~ × 60. Different volume constraints are examined, namely 50%, 40% and 30%.

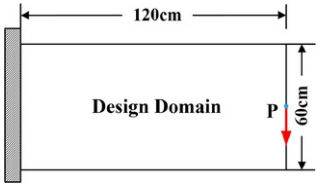

Fig. 10 Design domain of third example.

alt-text: Fig. 10.

The initial design and optimized topologies with different volume constraints by the iPLSM are given in Fig. 11, and their FRF curves are shown in Fig. 12. Obviously, the resonance peaks are moved outside the excitation frequency range to avoid the drastic vibration. When comparing to the initial design, considerable reductions on structural frequency responses of the optimal designs are observed. In addition, it can be seen that the design with a lower volume fraction has an inferior dynamic stiffness, which is similar to the static stiffness optimization problem [10,48]. For comparison, the optimal results by respectively using the PLSM-1, PLSM-2 and iPLSM are given in Table 4. It is clear that the PLSM-1 always takes more iterations but achieves a worse dynamic compliance. Moreover, the iPLSM achieves the same optimized designs but considerably reduce the computer cost per step when comparing to the PLSM-2. It illustrates that the iPLSM method has very limited impact on the Gaussian RBF interpolation accuracy when dealing with the global frequency response optimization. In regards to both the optimization efficiency and effectiveness, the iPLSM performs best amongst the three methods.

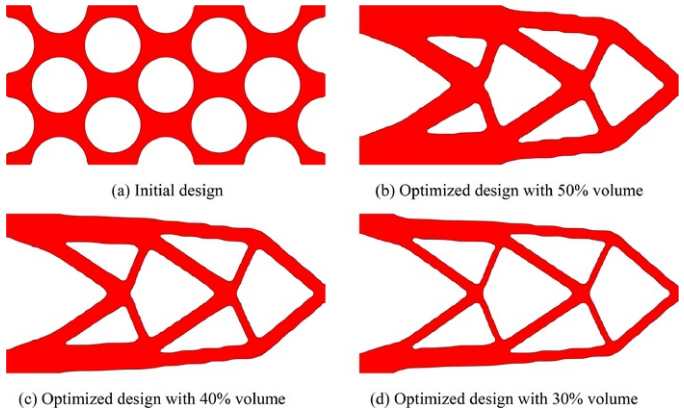

Fig. 11 Initial design and optimized designs of third example under different volume constraints.

alt-text: Fig. 11.

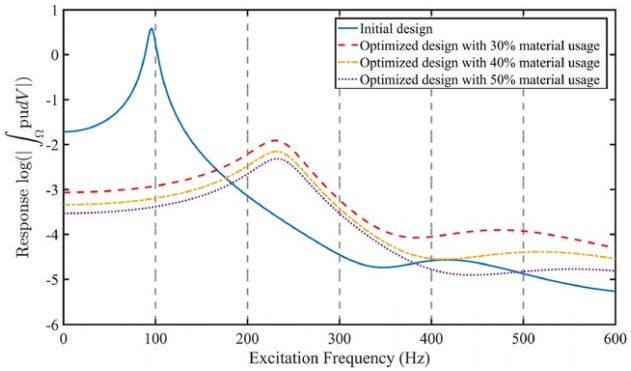

Fig. 12 FRF of initial design and optimized designs.

alt-text: Fig. 12.

Table 4 Comparison of different methods in 2D global frequency response optimization.

alt-text: Table 4

Method	Sparsity of matrix $\mathbf{A}$ or $\widetilde{\mathbf{A}}_s$	Volume constraint	Time per step	Iterations	Objective
iPLSM	99.59%	50%	26.3 s	112	1.1863
PLSM-1	99.26%	50%	26.5 s	165	1.2081
PLSM-2	0%	50%	69.8 s	112	1.1863
iPLSM	99.59%	40%	26.2 s	160	1.4370
PLSM-1	99.26%	40%	26.5 s	220	1.4926
PLSM-2	0%	40%	69.9 s	160	1.4370
iPLSM	99.59%	30%	26.3 s	176	1.8928
PLSM-1	99.26%	30%	26.4 s	260	1.9822

PLSM-2	0%	30%	69.8 s	176	1.8928

6.4 Local frequency response optimization of 3D structure

The design domain is given in Fig. 13. Both ends of the 3D beam are fixed, and a concentrated force $50000e^{j\omega T}$ N within Ω_{freq} = [0 Hz, 400 Hz] is applied at the middle point of the lower face. The structure is discretized with ~~12~~ 12 ~~×~~ × ~~12~~ 12 ~~×~~ × 48 eight-node elements, and only ~~12~~ 12 ~~×~~ × ~~6~~ 6 ~~×~~ × 48 FEs are taken into consideration due to the geometrical symmetry. The whole design domain is assumed to be occupied by a sort of base material with a lower density ρ_{min} = 0.78 g/cm^3. The objective function is to minimize the frequency response at point **P** by reinforcing the basic structure with a given amount of higher-density materials (e.g. ρ = 7.8 g/cm^3). The maximum reinforcement material usage is 30%.

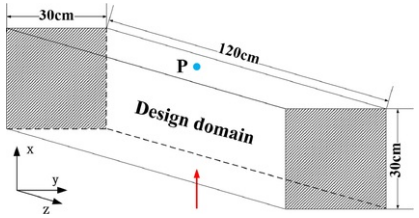

Fig. 13 Design domain of fourth example.

alt-text: Fig. 13.

The iPLSM is firstly applied. The zero level set contours of the 3D beam are plotted in Fig. 14, in which the low density material is indicated as grey, while the reinforcement material is denoted as red. It can be seen that a smooth geometrical surface is obtained through the evolving of structural shapes and topologies. For comparison, the optimal results obtained by the PLSM-1 and PLSM-2 are provided in Fig. 15 and Table 5. It is obvious that the iPLSM can achieve a much better objective with less iteration numbers when comparing to the PLSM-1, while have a similar objective with a considerable increment in optimization efficiency when comparing to the PLSM-2. More importantly, when comparing with the conventional PLSM (i.e. PLSM-1), the iPLSM can significantly improve the dynamic performance (13% improvement) of the design in 3D scenario. It confirms that the proposed method is more efficient and effective in dealing with 3D optimization design problem.

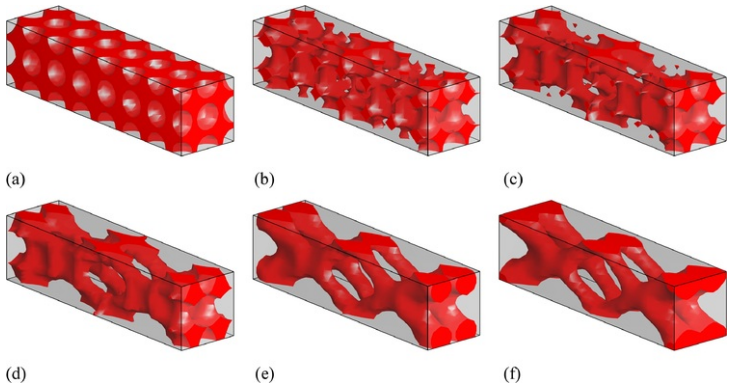

Fig. 14 Evolution of structural boundary of fourth example: (a) initial design; (b) step 15; (c) step 20; (d) step 25; (e) step 50; (f) optimized design.

alt-text: Fig. 14.

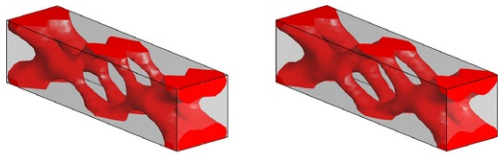

(a) (b)

Fig. 15 Optimal designs of fourth example: (a) PLSM-1; (b) PLSM-2.

alt-text: Fig. 15.

Table 5 Comparison of different methods in fourth example.

alt-text: Table 5

Method	Mesh	Size of matrix **A**	Sparsity of matrix $\mathbf{A}$ or $\widetilde{\mathbf{A}}_s$	Time per step	Iterations	Objective
iPLSM	12 12 × × 6 6 × × 48	4459 4459 × × 4459	96.15%	236.3 s	96	2.1872e−3
PLSM-1	12 12 × × 6 6 × × 48	4459 4459 × × 4459	89.06%	241.6 s	108	2.5075e−3
PLSM-2	12 12 × × 6 6 × × 48	4459 4459 × × 4459	0%	269.6 s	96	2.1864e−3

6.5 Global frequency response optimization of 3D structure

The design domain is shown in Fig. 16, and a set of excitation loads $100e^{j\omega T_H}$N with Ω_{freq}=[0 Hz, 100 Hz] are uniformly applied along the central line on the top face of the structure. The structure is discretized with 20 20 × × 12 12 × × 100 elements, and only 20 20 × × 6 6 × × 100 FEs are taken into consideration due to the geometrical symmetry. The objective function is to minimize the structural dynamic compliance. Two volume constraints, i.e. 40% and 20%, are considered.

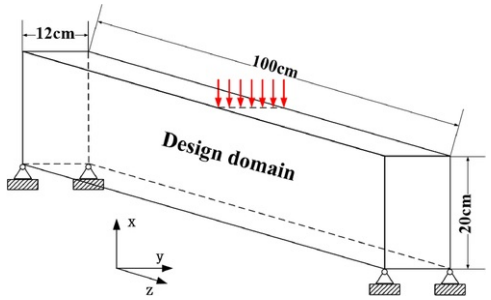

Fig. 16 Design domain of fifth example.

alt-text: Fig. 16.

For comparison, the design results with different volume constraints by using the iPLSM and PLSM-1 are presented in Fig. 17 and Table 6, and their FRF curves are shown in Fig. 18. Comparing with the PLSM-1, the proposed method always takes fewer iterations to search for a design with a much better dynamic performance (respectively 54% and 98% improvements). Moreover, it is of great interest to see that the PLSM-1 fails to obtain a feasible design when the volume constraint is kept at a lower level (i.e. 20%). It is because that the CSRBF may not provide adequate interpolation accuracy to approximate the moving boundary during the optimization, especially when dealing with 3D optimization problems with lower volume fractions. Nevertheless, the iPLSM is still able to find an optimal design with a low volume fraction due to its high-accuracy interpolation mechanism. This demonstrates that the proposed method is more efficient and effective than the conventional PLSM.

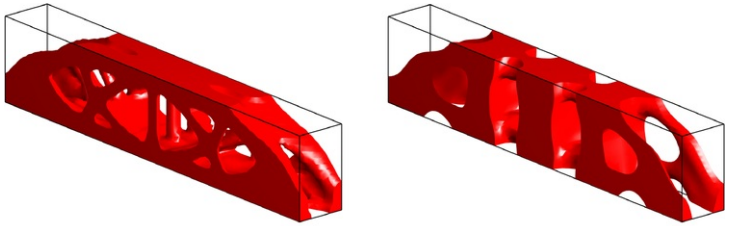

(a) Designs with 40% material usage: iPLSM (Left); PLSM-1 (Right)

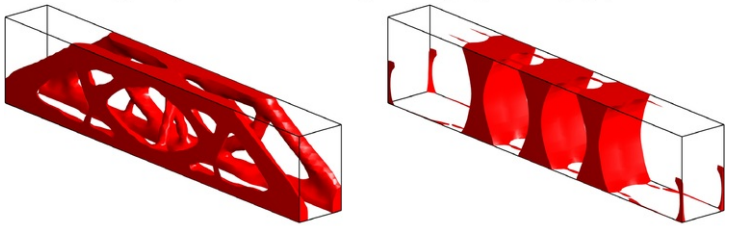

(b) Designs with 20% material usage: iPLSM (Left); PLSM-1 (Right)

Fig. 17 Design results of fifth example using different methods.

alt-text: Fig. 17.

Table 6 Comparison of different methods in fifth example.

alt-text: Table 6

Method	Size of matrix **A**	Sparsity of matrix $\mathbf{A}$ or $\tilde{\mathbf{A}}_s$	Volume	Time per setp	Iterations	Objective
iPLSM	14,~~847~~ 847 ~~×~~ × 14,847	99.38%	40%	585.6 s	116	34.7718
PLSM-1	14,~~847~~ 847 ~~×~~ × 14,847	96.34%	40%	592.2 s	400	75.8112
iPLSM	14,~~847~~ 847 ~~×~~ × 14,847	99.38%	20%	585.8 s	142	59.1339
PLSM-1	14,~~847~~ 847 ~~×~~ × 14,847	96.34%	20%	592.4 s	215	2703.0524

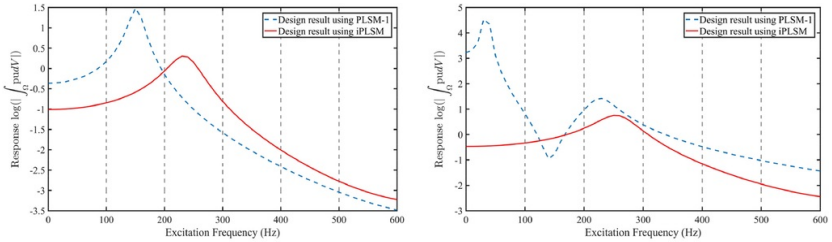

(a) (b)

Fig. 18 FRF curves of optimized designs: (a) volume constraint is 40%; (b) volume constraint is 20%.

alt-text: Fig. 18.

From above numerical examples, it is seen that the proposed method can benefit the structural topology optimizations. In particular, the iPLSM can produce smooth structure boundary and clear design geometry that can facilitate the optimized results to be directly integrated into the commercial software for analysis or fabrication purposes. Furthermore, the proposed method can simultaneously implement the shape and topology optimizations via structural boundary merging and splitting. Actually, the iPLSM-based formulation can be directly solved by the well-established gradient-based algorithms, which makes this method more general and easy-to-implement for different

optimization problems.

7 Conclusions

This paper has proposed an efficient iPLSM to minimize the frequency response of structures within a given excitation frequency range. In this method, a new parameterization mechanism is developed: (1) the level set function is approximated by using the Gaussian RBF, and (2) the DWT is introduced to compress the full matrix arisen from the interpolation. Then, the structural shape and topology changes are efficiently driven by the parameterization method. The design sensitivities of the objective function and constraint are obtained, to enable the iterative update of the design variables by using the gradient-based OC algorithm. Several 2D and 3D numerical examples regarding with both the local and global frequency response optimizations have been used to demonstrate the merits of the proposed method. Firstly, the iPLSM considerably increases the optimization efficiency and effectiveness by comparing to the conventional PLSM, especially for 3D problems. Secondly, it can simultaneously maintain the unique merits while overcome numerical difficulties of conventional LSMs. Thirdly, the proposed method can provide effective reduction on vibrations with different objective functions and boundary conditions. Finally, the iPLSM is general and suitable for different types of advanced topology optimization problems.

Acknowledgements

This research is supported by National Natural Science Foundation of China (51705166 and 11502083), National Basic Scientific Research Program of China(JCKY2016110C012), China Postdoctoral Science Foundation (2017M612446), Australian Research Council (ARC) - Discovery Projects (160102491), and the Open Research Project of “The State Key Laboratory of Digital Manufacturing Equipment and Technology”, Huazhong University of Science and Technology (DMETKF2015010), Wuhan, China.

References

[1] AGM Michell, The limit of economy of material in frame structures, *Philos Mag* **8**, 1904, 589–597.

[2] BHV Topping, Shape optimization of skeletal structures: ~~A~~a review, *J Struct Eng* **109**, 1983, 1933–1951.

[3] HL Cox, The design of structures of least weight, 1965, Pergamon Press; Oxford.

[4] W Hemp and HSY Chan, Optimum design of pin-jointed frameworks, 1966, Her Majesty's Stationary Office, London: R. & M. 3632.

[5] W Hemp, Optimum structures, 1973, Clarendon Press; Oxford.

[6] HSY Chan, The design of michell optimum structures, 1960, Cranfield: College of Aeronautics, Technical report.

[7] W Prager and GIN Rozvany, Optimal layout of grillages, *J Struct Mech* **5**, 1977, 1–18.

[8] GD Cheng and N Olhoff, An investigation concerning optimal design of solid elastic plates, *Int J Solids Struct* **17**, 1981, 305–323.

[9] GD Cheng and N Olhoff, Regularized formulation for optimal design of axisymmetric plates, *Int J Solids Struct* **18**, 1982, 153–169.

[10] MP Bendsøe and O Sigmund, Topology optimization: theory, methods, and applications, 2003, Springer; Berlin, Heidelberg.

[11] O Sigmund and K Maute, Topology optimization approaches: a comparative review, *Struct Multidiscip Optim* **48**, 2013, 1031–1055.

[12] MP Bendsøe and N Kikuchi, Generating optimal topologies in structural design using a homogenization method, *Comput Methods Appl Mech Engrg* **71**, 1988, 197–224.

[13] M Zhou and GIN Rozvany, The COC algorithm, part II: ~~T~~topological, geometry and generalized shape optimization, *Comput Methods Appl Mech Engrg* **89**, 1991, 309–336.

[14] MP Bendsøe and O Sigmund, Material interpolation schemes in topology optimization, *Arch Appl Mech* **69**, 1999, 635–654.

[15] YM Xie and GP Steven, A simple evolutionary procedure for structural optimization, *Comput Struct* **49**, 1993, 885–896.

[16] S Osher and JA Sethian, Fronts propagating with curvature-dependent speed-algorithms based on Hamilton–Jacobi formulations, *J Comput Phys* **79**, 1988, 12–49.

[17] JA Sethian and A Wiegmann, Structural boundary design via level set and immersed interface methods, *J Comput Phys* **163**, 2000, 489–528.

[18] S Osher and RP Fedkiw, Level set methods and dynamic implicit surface, 2002, Springer; New York.

[19] MY Wang, XM Wang and DM Guo, A level set method for structural topology optimization, *Comput Methods Appl Mech Engrg* **192**, 2003, 227–246.

[20] G Allaire, F Jouve and AM Toader, Structural optimization using sensitivity analysis and a level-set method, *J Comput Phys* **194**, 2004, 363–393.

[21] NP van Dijk, K Maute, M Langelaar and F van Keulen, Level-set methods for structural topology optimization: a review, *Struct Multidiscip Optim* **48**, 2013, 437–472.

[22] G Allaire and F Jouve, A level-set method for vibration and multiple loads structural optimization, *Comput Methods Appl Mech Engrg* **194**, 2004, 3269–3290.

[23] MY Wang and XM Wang, "Color" level sets: a multi-phase method for structural topology optimization with multiple materials, *Comput Methods Appl Mech Engrg* **193**, 2004, 469–496.

[24] T Yamada, K Izui, S Nishiwaki and A Takezawa, A topology optimization method based on the level set method incorporating a fictitious interface energy, *Comput Methods Appl Mech Engrg* **199**, 2010, 2876–2891.

[25] SW Zhou, W Li, GY Sun and Q Li, A level-set procedure for the design of electromagnetic metamaterials, *Opt Express* **18**, 2010, 6693–6702.

[26] SK Chen and W Chen, A new level-set based approach to shape and topology optimization under geometric uncertainty, *Struct Multidiscip Optim* **44**, 2011, 1–18.

[27] NP van Dijk, M Langelaar and F van Keulen, Explicit level-set-based topology optimization using an exact Heaviside function and consistent sensitivity analysis, *Int J Numer Methods Eng* **91**, 2012, 67–97.

[28] X Guo, W Zhang and W Zhong, Explicit feature control in structural topology optimization via level set method, *Comput Methods Appl Mech Engrg* **272**, 2014, 354–378.

[29] PD Dunning and HA Kim, Introducing the sequential linear programming level-set method for topology optimization, *Struct Multidiscip Optim* **51**, 2015, 631–643.

[30] K. Svanberg, The method of moving asymptotes: a new method for structural optimization, *Int J Numer Methods Eng* **24**, 1987, 359–373.

[31] T Belytschko, SP Xiao and C Parimi, Topology optimization with implicitly function and regularization, *Int J Numer Methods Eng* **57**, 2003, 1177–1196.

[32] Q Xia, MY Wang, SY Wang and SK Chen, Semi-Lagrange method for level-set-based structural topology and shape optimization, *Struct Multidiscip Optim* **31**, 2006, 419–429.

[33] JZ Luo, Z Luo, LY Tong and MY Wang, A semi-implicit level set method for structural shape and topology optimization, *J Comput Phys* **227**, 2008, 5561–5581.

[34] MD Zhou and MY Wang, A semi-Lagrangian level set method for structural optimization, *Struct Multidiscip Optim* **46**, 2012, 487–501.

[35] Z Luo, MY Wang, SY Wang and P Wei, A level set-based parameterization method for structural shape and topology optimization, *Int J Numer Methods Eng* **76**, 2008, 1–26.

[36] Z Luo, LY Tong and Z Kang, A level set method for structural shape and topology optimization using radial basis functions, *Comput Struct* **87**, 2009, 425–434.

[37] YQ Wang, Z Luo, N Zhang and Z Kang, Topological shape optimization of microstructural metamaterials using a level set method, *Comput Mater Sci* **87**, 2014, 178–186.

[38] MD Buhmann, *Radial basis functions: theory and implementations, Cambridge monographs on applied and computational mathematics* **12**, 2004, Cambridge University Press; New York.

[39] H Wendland, Computational aspects of radial basis function approximation, 2005, Elsevier BV.

[40] J Ravnik, L Škerget and M Hriberšek, The wavelet transform for BEM computational fluid dynamics, *Eng Anal Bound Elem* **28**, 2004, 1303–1314.

[41] K Chen, Discrete wavelet transforms accelerated sparse preconditioners for dense boundary element systems, *Electron Trans Numer Anal* **8**, 1999, 138–153.

[42] NL Pedersen, Maximization of eigenvalues using topology optimization, *Struct Multidiscip Optim* **20**, 2000, 2–11.

[43] TS Kim and YY Kim, MAC-based mode-tracking in structural topology optimization, *Comput Struct* **74**, 2000, 375–383.

[44] Y Maeda, S Nishiwaki, K Izui, M Yoshimura, K Matsui and K Terada, Structural topology optimization of vibrating structures with specified eigenfrequencies and eigenmode shapes, *Int J Numer Methods Eng* **67**, 2006, 597–628.

[45] JB Du and N Olhoff, Topological design of freely vibrating continuum structures for maximum values of simple and multiple eigenfrequencies and frequency gaps, *Struct Multidiscip Optim* **34**, 2007, 91–110.

[46] ZH Li, Q Xia and TL Shi, Eliminate localized eigenmodes in level set based topology optimization for the maximization of the first eigenfrequency of vibration, *Adv Eng Softw* **107**, 2017, 59–70.

[47] ZD Ma, N Kikuchi and I Hagiwara, Structural topology and shape optimization for a frequency response problem, *Comput Mech* **13**, 1993, 157–174.

[48] ZD Ma, N Kikuchi and HC Cheng, Topological design for vibrating structures, *Comput Methods Appl Mech Engrg* **121**, 1995, 259–280.

[49] CS Jog, Topology design of structures subjected to periodic loading, *J Sound Vibr* **253**, 2002, 687–709.

[50] D Tcherniak, Topology optimization of resonating structures using SIMP method, *Int J Numer Methods Eng* **54**, 2002, 1605–1622.

[51] N Olhoff and JB Du, Generalized incremental frequency method for topological design of continuum structures for minimum dynamic compliance subject to forced vibration at a prescribed low or high value of the excitation frequency, *Struct Multidiscip Optim* **54**, 2016, 1113–1141.

[52] XP Zhang, Z Kang and WB Zhang, Robust topology optimization for dynamic compliance minimization under uncertain harmonic excitations with inhomogeneous eigenvalue analysis, *Struct Multidiscip Optim* **54**, 2016, 1469–1484.

[53] JS Jensen, Topology optimization of dynamics problems with Padé approximants, *Int J Numer Methods Eng* **72**, 2007, 1605–1630.

[54] GH Yoon, Structural topology optimization for frequency response problem using model reduction schemes, *Comput Methods Appl Mech Engrg* **199**, 2010, 1744–1763.

[55] L Shu, MY Wang, ZD Fang, ZD Ma and P Wei, Level set based structural topology optimization for minimizing frequency response, *J Sound Vibr* **330**, 2011, 5820–5834.

[56] JH Rong, ZL Tang, YM Xie and FY Li, Topological optimization design of structures under random excitations using SQP method, *Eng Struct* **56**, 2013, 2098–2106.

[57] H Liu, WH Zhang and T Gao, A comparative study of dynamic analysis methods for structural topology optimization under harmonic force excitations, *Struct Multidiscip Optim* **51**, 2015, 1321–1333.

[58] G Beylkin, R Coifman and V Rokhlin, Fast wavelet transforms and numerical algorithms, *Commun Pure Appl Math* **44**, 1991, 141–183.

[59] J Jung, J Hyun, S Goo and S Wang, An efficient design sensitivity analysis using element energies for topology optimization of a frequency response problem, *Comput Methods Appl Mech Eng* **296**, 2015, 196–210.

[60] KK Choi and NH Kim, Structural sensitivity analysis and optimization - linear systems, 2005, Springer; New York.

[61] R Ohayon and C Soize, Structural acoustics and vibration, 1998, Academic Press; New York.

[62] XP Zhang and Z Kang, Topology optimization of piezoelectric layers in plates with active vibration control, *J Intell Mater Syst Struct* **25**, 2014, 697–712.

[63] J Sokolowski and JP Zolesio, Introduction to shape optimization: shape sensitivity analysis, 1992, Springer-Verlag; New York.

[64] M Bruyneel and P Duysinx, Note on topology optimization of continuum structures including self-weight, *Struct Multidiscip Optim* **29**, 2005, 245–256.

[65] JH Zhu, P Beckers and WH Zhang, On the multi-component layout design with inertial force, *J Comput Appl Math* **234**, 2010, 2222–2230.

[66] T Belytschko, C Parimi, N Moes, N Sukumar and S Usui, Structured extended finite element methods for solids defined by implicit surfaces, *Int J Numer Methods Eng* **56**, 2002, 609–635.

[67] B Bourdin, Filters in topology optimization, *Int J Numer Methods Eng* **50**, 2001, 2143–2158.

[68] O Sigmund, A 99 line topology optimization code written in Matlab, *Struct Multidiscip Optim* **21**, 2001, 120–127.

[69] GH Yoon, Toward a multifrequency quasi-static Ritz vector method for frequency-dependent acoustic system application, *Int J Numer Methods Eng* **89**, 2012, 1451–1470.

Highlights

- An improved parametric level set method is proposed.
- The discrete wavelet transform is used to compress the Gaussian RBF-based interpolation matrix.
- Both self and non-self adjoint problems for global and local frequency responses are investigated.
- The efficiency and effectiveness of the proposed method are verified.

Queries and Answers

Query: Please confirm that givennames and surnames have been identified correctly.
Answer: Yes

Query: Fig. [9] has been submitted as color image; however, the caption has been reworded to ensure that it is meaningful when your article is reproduced both in colour and in black and white. Please check and correct if necessary.
Answer: yes, thanks

Query: Please check funding information and confirm its correctness.
Answer: yes, thanks

Query: Please check funding information and confirm its correctness.
Answer: yes, thanks